 CMES, vol.82, no.1, pp.55-81, 2011

Topology Optimization of a Linear Piezoelectric Micromotor Using the Smoothed Finite Element Method

Mohsen Sadeghbeigi Olyaie[1], Mohammad Reza Razfar[2], Semyung Wang[3] Edward J. Kansa[4]

Abstract: This paper presents the topology optimization design for a linear micromotor, including multitude cantilever piezoelectric bimorphs. Each microbeam in the mechanism can be actuated in both axial and flexural modes simultaneously. For this design, we consider quasi-static and linear conditions, and the smoothed finite element method (S-FEM) is employed in the analysis of piezoelectric effects. Certainty variables such as weight of the structure and equilibrium equations are considered as constraints during the topology optimization design process, then a deterministic topology optimization (DTO) is conducted. To avoid the overly stiff behavior in FEM modeling, a relatively new numerical method known as the cell-based smoothed finite element method (CS-FEM, as a branch of S-FEM) is introduced for our DTO problem. The topology optimization procedure is implemented using a solid isotropic material with a penalization (SIMP) approximation and a method of moving asymptotes (MMA) optimizer. Because of the higher efficiency and accuracy of S-FEMs with respect to standard FEMs, numerical results of our DTO analysis using a softer CS-FEM are substantially improved, compared to FEMs using quadrilateral elements (Q4) and triangular elements (T3) when the same sets of nodes are used.

Keywords: Topology Optimization, Smoothed Finite Element Method, Linear Micromotor, Piezoelectric

[1] Corresponding author, Department of Mechanical Engineering, Amirkabir University of Technology, Tehran, Iran, Email: m.sadeghbeigi@aut.ac.ir

[2] Department of Mechanical Engineering, Amirkabir University of Technology, Tehran, Iran, Email: razfar@aut.ac.ir

[3] School of Mechatronics, Gwangju Institute of Science and Technology, Gwangju, South Korea, Email: smwang@gist.ac.kr

[4] Department of Mechanical and Aeronautical Engineering, University of California-Davis, Davis, CA 95616, USA, Email: ejkansa@ucdavis.edu

1 Introduction

Because of various advanced applications of actuators in industry, the dimensions of linear actuators are gradually being reduced to even beyond the range of microelectromechanical systems (MEMS) devices. Among actuation mechanisms, piezoelectric microactuators have been found to be superior in providing linear actuation forces and nanometer positioning, see Ueha and Tomikawa (1993). The ability to make use of the piezoelectric effect was first discovered by the Curie brothers in 1880; the piezoelectric effect can have both direct (sensing) and inverse (actuation) effects, see Yang (2006). Via the direct effect, these materials can produce electric charges under mechanical stresses, and based on the inverse effect the materials are actuated through the application of an electric field.

To obtain an optimum design of piezoelectric structures requires a systematic approach to reduce the dimensions of these materials to increase their efficiency, see Frecker (2003); Irschik (2002). Currently, the most common strategy for designing these structures is the deterministic optimization model, see Arora (2004). This optimization technique determines the optimum solution using fixed design parameters such as volume (weight), geometry, material property, or stress level.

Topology optimization is a branch of optimization methods that are used to determine optimal material distributions for a given design domain, see Bendsoe and Sigmund (2003). The start of the topology optimization concept goes back to 1904, at which time Michell minimized the weight of a structure under stress constraints, see Spillers and MacBain (2009). However, fast development in the topology optimization field started after the landmark paper of Bendsoe and Kikuchi in 1988.

Topology optimization using a solid isotropic material with a penalization (SIMP) approximation is the simplest and most popular technique; see Rozvany, Zhou and Birker (1992). This technique penalizes the intermediate density of each element, as a design variable, to an analogue value using power law approximations, see Bendsoe (1989). Design variables in the optimization process can also be updated through some algorithms such as sequence linear programming (SLP) or sequence quadratic programming (SQP), see Nocedal and Wrigh (2006). For example, Svanberg (1987) proposed a powerful optimizer tool known as the method of moving asymptotes (MMA) for this purpose. This optimizer usually has sufficient compatibility with multi- and nonlinear constraints.

A simple numerical optimization procedure is shown in figure 1. In the figure, the major time-consuming task under the updating loop for the optimization (or topology optimization) procedure needs to be handled by a stable and efficient numerical method such as the finite element method (FEM). For piezoelectric analyses, due to the overly stiff behavior of the FEM obtained from the overestimation of

the stiffness matrix, results usually have low stress accuracy and the solution is sensitive to element distortions, see Benjeddou (2000); Allik and Hughes (1970). To overcome these drawbacks, finite element methods such as the piezoelectric finite element with drilling degrees of freedom, see Long, Loveday and Groenwold (2006), hybrid formulations, see Sze, Yang and Yao (2004), and meshless methods such as the meshless point collocation method (PCM) and radial point interpolation method (RPIM) have been developed, see Ohs and Aluru (2001); Liu, Dai, Lim and Gu (2003).

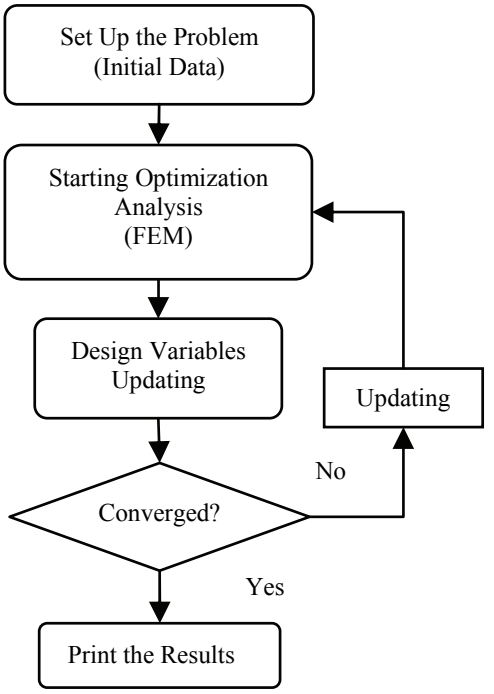

Figure 1: Typical flowchart for a numerical optimization

A method that combines parts of the standard FEM and meshless techniques, see Chen, Wu and Yoon (2001), called the smoothed finite element method (S-FEM), was developed by Liu, Dai and Nguyen in 2007. This method states that numerical analyses of static and dynamic problems through S-FEMs are always more stable than standard FEMs, due to softening effects provided by smoothing operations in the S-FEM, see Bordas, Rabczuk, Hung, Nguyen, Natarajan, Bog, Quan and Hiep (2010). As such, the S-FEM numerical results are often found to be even

more accurate than those of standard FEMs with the same degrees of freedom, see Liu, Nguyen and Lam (2009); Liu and Nguyen (2010); Liu, Nguyen, Dai and Lam (2007); Nguyen, Liu, Nguyen and Nguyen (2009); Liu, Nguyen and Nguyen (2010).

Static and eigenvalue models of piezoelectric structures using an edge-based S-FEM were then developed by Nguyen-Xuan, Liu, Nguyen and Nguyen in 2009. Their results showed good agreement with analytical solutions, and also had more accuracy than standard FEMs.

To date, most investigations on piezoelectric topology optimizations, such as that by Silva and Kikuchi in 1999; Silva in 2003; Begg and Liu in 2000; Carbonari, Nader and Silva in 2006; Carbonari, Silva and Nishiwaki in 2005; Kogl and Silva in 2005; Kang and Wang in 2010; Donoso and Sigmund in 2009; Kim J.E, Kim D.S, Ma and Kim Y.Y in 2010, have focused on optimizations through standard FEM algorithms. However, because of the important role of finite element models on the final optimization results, the topology optimization of the considered piezoelectric micromotor, proposed by Friend, Umeshima, Ishii, Nakamura and Ueha in 2004, using the softer CS-FEM will be further discussed in this paper.

The remainder of this paper is organized as follows. The design concept of an actuator will be discussed in section 2. The S-FEM and cell-based smoothed finite element method are then introduced in section 3. Next, the framework of topology optimization will be explained in section 4, and in section 5 the problem algorithm will be explained. In section 6, the DTO numerical results of this micromotor analysis based on Q4-FEM, T3-FEM, and CS-FEM will be compared, examined, and discussed in detail. Finally, conclusions of this research will be briefly explained.

2 Concept design of the used piezoelectric linear micromotor

Recently, linear actuators have been used in various engineering applications for fields such as aerospace, robotics, optics, and medical science. Because these actuators need to fit into small devices such as cell phones, microrobotics, and those used in microsurgeries, they are moving toward and beyond MEMS size.

Many smart materials such as shape memory alloys, magnetostrictives, electrostrictives, and piezoelectric materials can be used for actuation in these systems, see Moskalik and Brei (1999). However, shape memory alloys usually have slow dynamic responses, electro- or magnetostrictives have nonlinear responses, and piezoelectric materials produce limit strains, see Moskalik and Brei (1999). Because of the rapid dynamic responses, large actuation force, and fairly linear behavior of piezoelectric materials, these materials are the preferred choices for various purposes, including actuation and vibration controls, see Irschik (2002). To overcome

limitations in displacement generation, different actuation architectures have been developed, including, see Moskalik and Brei (1999): 1) internally leveraged amplifiers such as bimorph cantilevers, and 2) externally leveraged mechanisms such as the X-frame and Moonie. The bimorph cantilever has been found to be capable of producing larger deflections than other configurations, see Wang, Zhang, Xu, Liu and Cross (1999).

The design concept of the linear micromotor used in this study is based on the axial and transverse motions of bimorph piezoelectric cantilevers, see Friend, Umeshima, Ishii, Nakamura and Ueha (2004). Figure 2 schematically shows the layout of these cantilever bimorphs and the operating mechanism of this linear motor. Detailed information about each bimorph can be seen in figure 3; in the figure, each beam includes an elastic material interface with low magnetic permeability (such as phosphor bronze), two piezoelectric layers with the same polarization direction, and finally some relevant electrodes for applying electric fields. The initial state of the piezoelectric beam is shown in figure 4(a). By applying an electric voltage on electrodes 2 and 4 (figure 4(b)), an axial displacement will be produced; by just applying a voltage on electrodes 1 and 3 a transverse movement is achievable (figure 4(c)). Finally, by applying an electric field simultaneously on all four electrodes, an elliptical motion will be generated (figure 4(d)). By creating a suitable phase shifting on the piezoelectric sequentially bimorphs, and then by generating a preload force on the system, a linear motion will be produced (figure 2). Recently, a Swedish company (PiezoMotor AB) has been commercially manufacturing this type of linear motor.

3 Cell-based smoothed finite element method formulations for piezoelectric problems

Based on the variational formulation for a two-dimensional piezoelectric structure, the energy functional (L) for the design domain (Ω) can be expressed as, see Benjeddou (2000); Allik and Hughes (1970); Nguyen X.H., Liu, Nguyen T.T. and Nguyen C.T. (2009):

$$L = \int_{\Omega} \left[\frac{1}{2}\rho \dot{\mathbf{U}}^{\mathrm{T}}\mathbf{U} - \frac{1}{2}\mathbf{S}^{\mathrm{T}}\mathbf{T} + \frac{1}{2}\mathbf{D}^{\mathrm{T}}\mathbf{E} + \mathbf{U}^{\mathrm{T}}\mathbf{F}_{\mathrm{S}} - \varphi\mathbf{Q}_{\mathrm{S}} \right] \mathrm{d}\Omega + \sum \mathbf{U}^{\mathrm{T}}\mathbf{F}_{\mathrm{P}} - \sum \varphi\mathbf{Q}_{\mathrm{P}} \quad (1)$$

where $\mathbf{U}$ and $\dot{\mathbf{U}}$ are the mechanical displacement and velocity, respectively, φ relates to the electric potential vector, $\mathbf{T}$ and $\mathbf{S}$ denote the stress and strain vectors, and $\mathbf{D}$ and $\mathbf{E}$ are the electric displacement and electric field vectors. In addition, $\mathbf{F}_{\mathrm{S}}$ and $\mathbf{F}_{\mathrm{P}}$ express the surface and point loads on the design domain, and $\mathbf{Q}_{\mathrm{S}}$, $\mathbf{Q}_{\mathrm{P}}$, and ρ are the surface and point electric charge loads and the density.

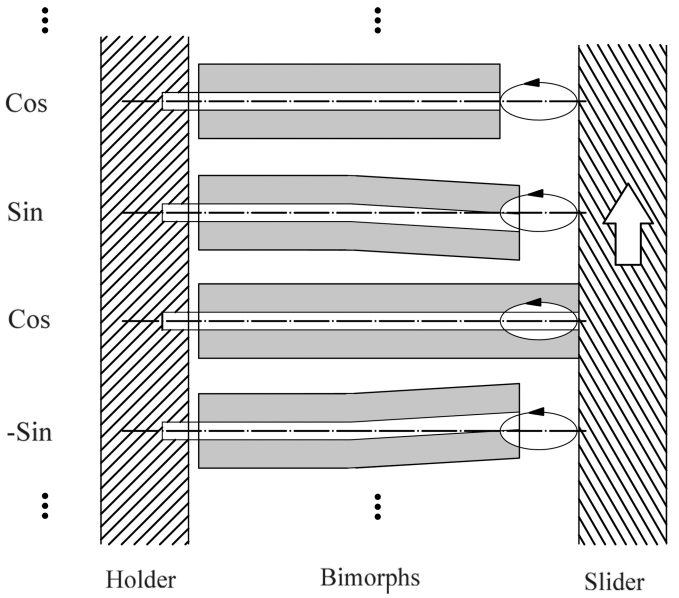

Figure 2: Operational mechanism of the considered piezoelectric linear micromotor, see Friend, Umeshima, Ishii, Nakamura and Ueha (2004)

For linear conditions, the matrix form of the constitutive equation for a piezoelectric structure can be written as:

$$\left\{ \begin{array}{c} \mathbf{T} \\ \mathbf{D} \end{array} \right\} = \begin{bmatrix} c_E & -e^{\mathrm{T}} \\ e & \varepsilon_s \end{bmatrix} \left\{ \begin{array}{c} \mathbf{S} \\ \mathbf{E} \end{array} \right\}. \tag{2}$$

In this equation, c_E, e, and ε_s are the elastic material property matrix at a constant electric field, and piezoelectric and dielectric matrices at a constant mechanical strain, respectively. For a standard FEM analysis, the compatibility relations between the strain-displacement and electric field-potential have the forms:

$$\mathbf{S} = \nabla \mathbf{U} \tag{3}$$

$$\mathbf{E} = -grad(\varphi) \tag{4}$$

When using a standard FEM, the unknown displacement and electric potential can be approximated as:

$$\mathbf{U}(x) = \sum_{I=1}^{n} \begin{bmatrix} \mathbf{N}_I(x) & 0 \\ 0 & \mathbf{N}_I(x) \end{bmatrix} \mathbf{U}_I; \quad \varphi(x) = \sum_{I=1}^{n} \mathbf{N}_I(x) \varphi_I \tag{5}$$

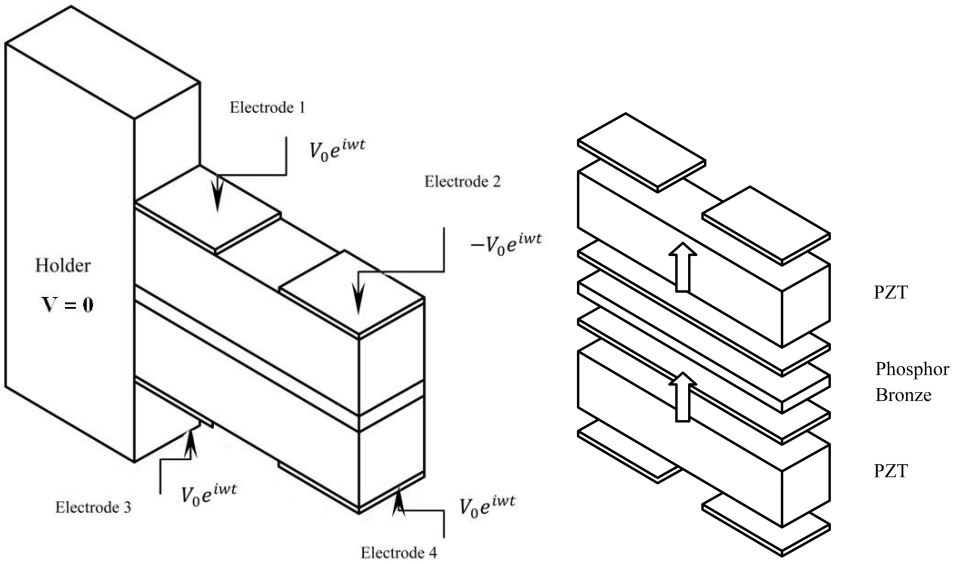

Figure 3: Bimorph beam used to construct the linear micromotor: (a) assembled, and (b) its components, see Friend, Umeshima, Ishii, Nakamura and Ueha (2004)

where n, $\mathbf{U}_I$, φ_I, and $\mathbf{N}_I(x)$ are the total number of nodes in the design domain, nodal displacement vector, nodal electric potential vector, and (linear) shape function, respectively. Substitution of Eq. (6) into Eqs. (3) and (4) leads to:

$$\mathbf{S} = \nabla \mathbf{U} = \sum_{I=1}^{n} \mathbf{B}_{UI} \mathbf{U}_I \tag{6}$$

$$\mathbf{E} = -grad(\varphi) = \sum_{I=1}^{n} \mathbf{B}_{\varphi I} \varphi_I \tag{7}$$

in which:

$$\mathbf{B}_{UI} = \begin{bmatrix} \mathbf{N}_{I,x} & 0 \\ 0 & \mathbf{N}_{I,y} \\ \mathbf{N}_{I,y} & \mathbf{N}_{I,x} \end{bmatrix}$$

and

$$\mathbf{B}_{\varphi\, I} = \begin{bmatrix} \mathbf{N}_{I,x} \\ \mathbf{N}_{I,y} \end{bmatrix}. \tag{8}$$

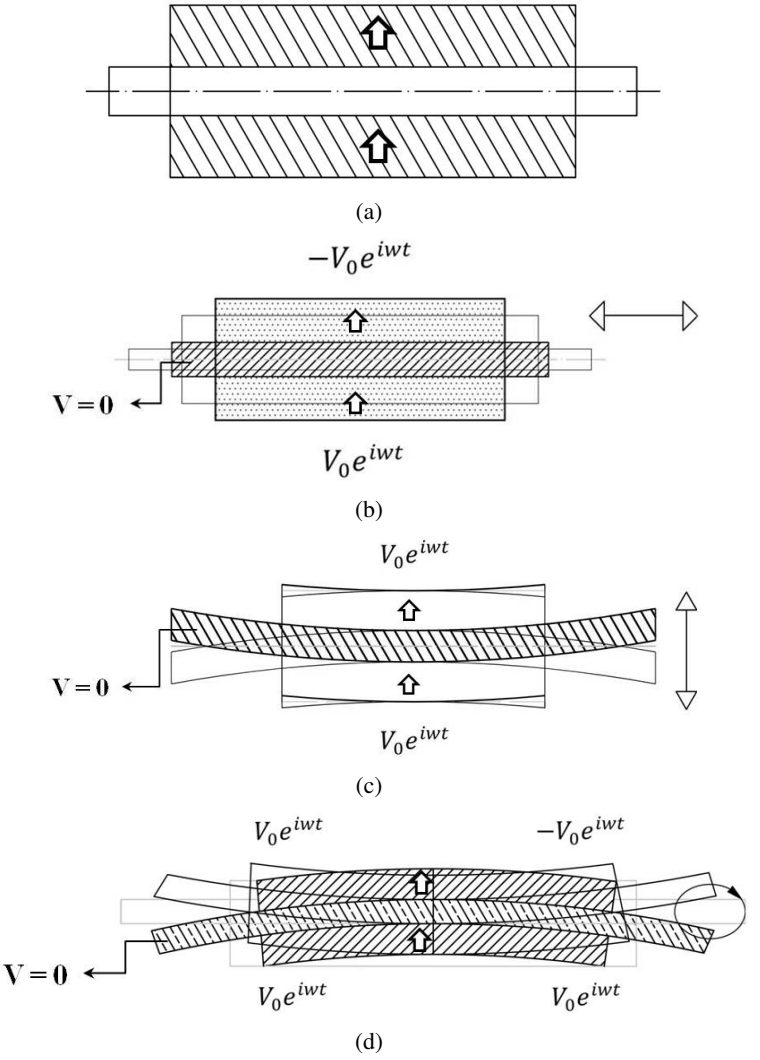

Figure 4: Vibration modes for a free-free piezoelectric bimorph: (a) initial state, (b) axial motion, (c) transverse motion, and (d) elliptical motion, see Friend, Umeshima, Ishii, Nakamura and Ueha (2004)

When the S-FEM is used, the problem domain is also discretized using the same elements as in the standard FEM, through a set of smoothing domains is created on top of the element mesh. The (compatible) strains given in Eq. (3) are then smoothed over each of the smoothing domains.

Based on the type of smoothing domain used, there are five possible S-FEM ver-

sions, see Liu and Nguyen (2010); Liu, Nguyen X.H. and Nguyen T.T. (2010): 1) cell-based S-FEM (CS-FEM), 2) node-based S-FEM (NS-FEM), 3) edge-based S-FEM (ES-FEM), 4) face-based S-FEM (FS-FEM), and 5) alpha-FEM.

The main difference between these versions is the type of smoothing domain used for strain smoothing. For example, in the ES-FEM the smoothing domains are constructed based on the edge of each standard triangular element; for NS-FEM, the smoothing domains are created according to the nodes and middle edge points of each element. The choice of the method generally depends on the requirement on the solution properties. For this study, because of the multi-material and multi-layer conditions CS-FEM is preferred.

For CS-FEM, the smoothing domains are constructed based on the cells located inside each element. These domains are linearly independent such that $\Omega = \cup_{c=1}^{n_c} \Omega^{(c)}$ and for each $i \neq j$, $\Omega^{(i)} \cap \Omega^{(j)} = \emptyset$. Here, Ω is the total design domain, $\Omega^{(i\ or\ j)}$ is the domain of $(i\ or\ j)^{th}$ smoothing domain, and n_c is the total number of cells inside the design domain. Figure 5 schematically presents the smoothing domains associated with the different number of cells (c) for a quadrilateral CS-FEM, see Liu, Nguyen X.H. and Nguyen T.T. (2010).

For each smoothing domain ($\Omega^{(c)}$) associated with a cell (c), the smoothed strains ($\tilde{\mathbf{S}}$) and smoothed electric fields ($\tilde{\mathbf{E}}$) for a piezoelectric structure can be written as:

$$\tilde{\mathbf{S}} = \int_{\Omega^{(c)}} \mathbf{S}(x)\chi^{(c)}(\mathbf{x})\mathrm{d}\Omega \tag{9}$$

$$\tilde{\mathbf{E}} = \int_{\Omega^{(c)}} \mathbf{E}(\mathbf{x})\chi^{(c)}(\mathbf{x})\mathrm{d}\Omega \tag{10}$$

where $\chi^{(c)}(\mathbf{x})$ is a smoothing function, simply chosen as:

$$\chi^{(c)}(\mathbf{x}) = \begin{cases} \frac{1}{A^{(c)}}, & x \in \Omega^{(c)} \\ 0, & x \notin \Omega^{(c)} \end{cases} \tag{11}$$

where $A^{(c)}$ is the area of the smoothing cell ($\Omega^{(c)}$) constructed by:

$$A^{(c)} = \int_{\Omega^{(c)}} \mathrm{d}\Omega. \tag{12}$$

Each element area is the summation of element cells areas, so:

$$A^e = \sum_{c}^{nSC} A_c \tag{13}$$

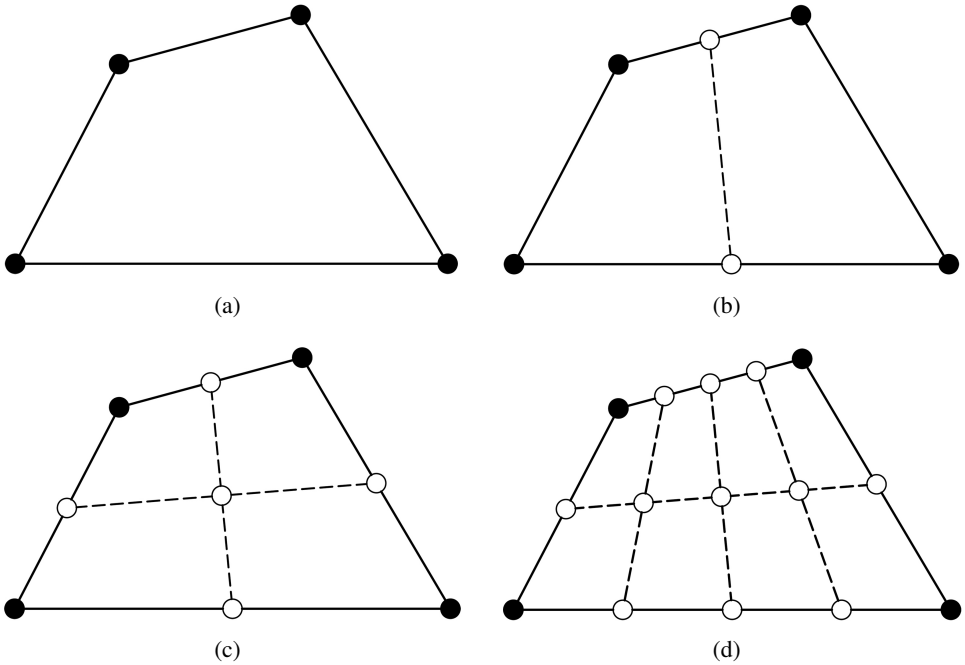

Figure 5: Smoothing domain (*SD*) concepts for the CS-FEM: (a) *1 SD*, (b) *2 SDs*, (c) *4 SDs,* and (d) 8SDs, see Liu, Nguyen X.H. and Nguyen T.T. (2010)

where *nSC* is the number of constructed cells for each element. Using the smoothing function (Eq. (12)) and by applying the divergence theorem, the smoothed strain and electric field will be changed to, see Liu, Nguyen X.H. and Nguyen T.T. (2010):

$$\tilde{\mathbf{S}} = \frac{1}{A^{(c)}} \int_{\Gamma^{(c)}} \mathbf{n}_u^{(c)} \mathbf{u}(\mathbf{x}) \mathrm{d}\Gamma = \sum_{I \in N_n} \tilde{\mathbf{B}}_{uI}(\mathbf{x}_c) \mathrm{d}_I \tag{14}$$

$$\tilde{\mathbf{E}} = -\frac{1}{A^{(c)}} \int_{\Gamma^{(c)}} \mathbf{n}_\varphi^{(c)} \varphi(\mathbf{x}) \mathrm{d}\Gamma = -\sum_{I \in N_n} \tilde{\mathbf{B}}_{\varphi I}(\mathbf{x}_c) \varphi_I \tag{15}$$

where $\Gamma^{(c)}$ is the boundary of the smoothing cell ($\Omega^{(c)}$), N_n is the number of element nodes, $\tilde{\mathbf{B}}_{uI}(\mathbf{x}_c)$ and $\tilde{\mathbf{B}}_{\varphi I}(\mathbf{x}_c)$ are the smoothed strain and smoothed electric field matricses on the domain ($\Omega^{(c)}$), respectively, and $\mathbf{n}_u^{(c)}$ and $\mathbf{n}_\varphi^{(c)}$ are the normal

outward vectors on the boundary ($\Gamma^{(c)}$), such that:

$$\mathbf{n}_u^{(c)} = \begin{bmatrix} \mathbf{n}_x^{(c)} & 0 \\ 0 & \mathbf{n}_y^{(c)} \\ \mathbf{n}_y^{(c)} & \mathbf{n}_x^{(c)} \end{bmatrix}, \quad \mathbf{n}_\varphi^{(c)} = \begin{bmatrix} \mathbf{n}_x^{(c)} & \mathbf{n}_y^{(c)} \end{bmatrix}^{\mathrm{T}}. \tag{16}$$

Note that the values of $\tilde{\mathbf{B}}_{uI}(\mathbf{x}_c)$ and $\tilde{\mathbf{B}}_{\varphi\, I}(\mathbf{x}_c)$ are:

$$\tilde{\mathbf{B}}_{uI}(\mathbf{x}_c) = \frac{1}{A^{(c)}} \begin{bmatrix} \int\limits_{\Gamma_b^{(c)}} \mathbf{N}_I \mathbf{n}_x \mathrm{d}\Gamma & 0 \\ 0 & \int\limits_{\Gamma_b^{(c)}} \mathbf{N}_I \mathbf{n}_y \mathrm{d}\Gamma \\ \int\limits_{\Gamma_b^{(c)}} \mathbf{N}_I \mathbf{n}_y \mathrm{d}\Gamma & \int\limits_{\Gamma_b^{(c)}} \mathbf{N}_I \mathbf{n}_x \mathrm{d}\Gamma \end{bmatrix}$$

$$= \frac{1}{A^{(c)}} \sum_{b=1}^{nb} \begin{bmatrix} \mathbf{N}_I(\mathbf{x}_b^g)\mathbf{n}_x^{(c)}(\mathbf{x}_b^g) & 0 \\ 0 & \mathbf{N}_I(\mathbf{x}_b^g)\mathbf{n}_y^{(c)}(\mathbf{x}_b^g) \\ \mathbf{N}_I(\mathbf{x}_b^g)\mathbf{n}_y^{(c)}(\mathbf{x}_b^g) & \mathbf{N}_I(\mathbf{x}_b^g)\mathbf{n}_x^{(c)}(\mathbf{x}_b^g) \end{bmatrix} l_b^{(c)} \tag{17}$$

$$\tilde{\mathbf{B}}_{\varphi\, I}(\mathbf{x}_c) = \frac{1}{A^{(c)}} \begin{bmatrix} \int\limits_{\Gamma^{(c)}} \mathbf{N}_I \mathbf{n}_x \mathrm{d}\Gamma \\ \int\limits_{\Gamma^{(c)}} \mathbf{N}_I \mathbf{n}_y \mathrm{d}\Gamma \end{bmatrix} = \frac{1}{A^{(c)}} \sum_{b=1}^{nb} \begin{bmatrix} \mathbf{N}_I(\mathbf{x}_b^g)\mathbf{n}_x^{(c)}(\mathbf{x}_b^g) \\ \mathbf{N}_I(\mathbf{x}_b^g)\mathbf{n}_y^{(c)}(\mathbf{x}_b^g) \end{bmatrix} l_b^{(c)} \tag{18}$$

where nb is the total number of boundary sections of ($\Gamma_b^{(c)}$),$\mathbf{x}_b^g$ is the midpoint(Gauss point) of each smoothing domain boundary segment ($\Gamma_b^{(c)}$), and $l_b^{(c)}$ is the length of each segment of ($\Gamma_b^{(c)}$). These equations show that unlike the standard FEMs, CS-FEM does not use the derivative of the shape functions for computing the smoothing (gradiant) strain and electric field matrices.

Similar to the standard FEM by applying Hamilton's principle, the general S-FEM discretized matrix form in a smoothing space for a complex form will be changed to, see Jensen (2009):

$$\tilde{\mathbf{M}}(\rho)\ddot{\hat{\mathbf{d}}} + \tilde{\mathbf{C}}(\rho)\dot{\hat{\mathbf{d}}} + \tilde{\mathbf{K}}(\rho)\hat{\mathbf{d}} = \hat{\mathbf{P}}(\rho, t). \tag{19}$$

In this equation, $\hat{d}$ and $\hat{\mathbf{P}}(\rho,t)$ are the transformed shapes of instantaneous displacement and load vectors, respectively. With a proportional damping assumption, the smoothing stiffness martix ($\tilde{\mathbf{K}}$) smoothing mass matrix ($\tilde{\mathbf{M}}$) and smoothing damping matrix ($\tilde{\mathbf{C}}$) will then become:

$$\tilde{\mathbf{K}} = \begin{bmatrix} \tilde{\mathbf{k}}_{uu} & \tilde{\mathbf{k}}_{u\varphi} \\ \tilde{\mathbf{k}}_{u\varphi} & \tilde{\mathbf{k}}_{\varphi\varphi} \end{bmatrix}; \quad \tilde{\mathbf{M}} = \begin{bmatrix} \mathbf{m} & 0 \\ 0 & 0 \end{bmatrix}; \quad \tilde{\mathbf{C}} = \alpha\tilde{\mathbf{M}} + \vartheta\tilde{\mathbf{K}} \tag{20}$$

where α and ϑ are the constant prescribed damping coefficients. The components of the smoothed stiffness matrix for each element domain and the mass matrix can be calculated as follows, see Dai, Liu and Nguyen (2007):

$$\tilde{\mathbf{K}}_{e(uu)} = \sum_{c}^{nSC} (\tilde{\mathbf{B}}_u^{(c)})^T c_E \tilde{\mathbf{B}}_u^{(c)} A^{(c)}, \tag{21}$$

$$\tilde{\mathbf{K}}_{e(u\varphi)} = \sum_{c}^{nSC} (\tilde{\mathbf{B}}_u^{(c)})^{\mathrm{T}} e^{\mathrm{T}} \tilde{\mathbf{B}}_\varphi^{(c)} A^{(c)}, \tag{22}$$

$$\tilde{\mathbf{K}}_{e(\varphi\varphi)} = -\sum_{c}^{nSC} (\tilde{\mathbf{B}}_\varphi^{(c)})^{\mathrm{T}} \varepsilon_s \tilde{\mathbf{B}}_\varphi^{(c)} A^{(c)}, \tag{23}$$

$$\mathbf{m} = \int_{\Omega} \rho \mathbf{N}_I^{\mathrm{T}} \mathbf{N}_I \mathrm{d}\Omega. \tag{24}$$

For a time-harmonic excitation problem, the load vector in Eq. (20) ($\hat{\mathbf{P}}(\rho,t)$) has the general form:

$$\hat{\mathbf{P}}(\rho,t) = \mathbf{f}(\rho)\mathrm{e}^{\mathrm{i}wt} \tag{25}$$

where $\mathbf{f}(\rho)$ is the magnitude of the applied load vector, w is the rotational frequency of the applied load, and (i) is the imaginary number in complex variables. For topology optimization applications, all the design parameters in Eq. (20) are functions of density of each element (ρ) as the design variable.

With this assumption, Eq. (20) can be converted to:

$$\tilde{\mathbf{M}}(\rho)\ddot{\hat{\mathbf{d}}} + \tilde{\mathbf{C}}(\rho)\dot{\hat{\mathbf{d}}} + \tilde{\mathbf{K}}(\rho)\hat{\mathbf{d}} = \mathbf{f}(\rho)\mathrm{e}^{\mathrm{i}wt}. \tag{26}$$

Note that the steady sate solution of Eq. (27) is:

$$\hat{\mathbf{d}}(t) = \hat{\mathbf{u}}(\rho)\mathrm{e}^{\mathrm{i}wt} \tag{27}$$

where $\hat{\mathbf{u}}(\rho)$ is the magnitude of the displacement vector in complex form. By this assumption, Eq. (27) yields:

$$\left[-w^2\tilde{\mathbf{M}}(\rho) + \mathrm{i}w\tilde{\mathbf{C}}(\rho) + \tilde{\mathbf{K}}(\rho)\right]\hat{\mathbf{u}} = \mathbf{f}(\rho). \tag{28}$$

Then, by introducing a dynamic stiffness matrix ($\tilde{\mathbf{G}}(\rho,w)$), an alternative general form of this equation becomes:

$$\tilde{\mathbf{G}}(\rho,w)\hat{\mathbf{u}} = \mathbf{f}(\rho) \tag{29}$$

with:

$$\tilde{\mathbf{G}}(\rho, w) = -w^2\tilde{\mathbf{M}}(\rho) + \mathrm{i}w\tilde{\mathbf{C}}(\rho) + \tilde{\mathbf{K}}(\rho). \tag{30}$$

After solving Eq. (30) through the CS-FEM analysis, the instantaneous displacement ($\mathbf{x}(t)$) and velocity ($\dot{\mathbf{x}}(t)$) can be respectively achieved as:

$$\mathbf{x}(t) = Real(\hat{\mathbf{u}}(\rho)\mathrm{e}^{\mathrm{i}wt}), \tag{31}$$

$$\dot{\mathbf{x}}(t) = Real(\mathrm{i}w\hat{\mathbf{u}}(\rho)\mathrm{e}^{\mathrm{i}wt}). \tag{32}$$

As can be seen in the above equations, only the calculation of the stiffness matrix in the CS-FEM method is different from the standard FEM computations.

The solution of the CS-FEM with $nSC = 1$ is equal to the standard FEM solution using reduced integration points (upper bound solution with flexible stiffness). If the number of smoothed domains for each element approaches infinity, the solution will approach the full integration standard FEM solution with (2×2) Gauss integration (lower bound solution with stiff stiffness). Finally, if $1 < nSC < \infty$ the CS-FEM model is always softer than the FEM using the same set of elements, and the CS-FEM solution (in strain energy) falls between the upper-bound and lower-bound FEM solutions of the force driving problems, see Liu, Nguyen, Dai and Lam (2007). Since the displacement conformity in this method is only valid along the edges of each cell, the computed stiffness matrices and displacements obtained through this method will be more flexible and more accurate than the standard FEM values, respectively, see Chen, Wu and Yoon (2001); Liu, Dai and Nguyen (2007); Liu, Nguyen, Dai and Lam (2007). In particular, for nonlinear problems, computations through this method have a faster convergence rate than for standard FEMs, though its computation time is longer than the standard FEM analysis, see Liu, Dai and Nguyen (2007); Liu, Nguyen, Dai and Lam (2007). In addition, because the CS-FEM does not use derivatives of shape functions, it is a type of weak form method, see Liu (2009).

4 Topology optimization

This technique determines the optimum material distribution required for a system to optimize an objective function, such as velocity, with respect to some defined constraints.

The general form of a DTO problem is, see Youn, Choi and Park (2003):

$$DTO: \begin{cases} \text{Optimize: an objective function} \\ \text{Constraints:} \begin{cases} \text{Equilibrium equations} \\ \text{Volume, cost or certainty constraints} \end{cases} \end{cases}. \tag{33}$$

Numerical approaches such as homogenization, see Bendsoe and Kikuchi (1988), and SIMP techniques, see Rozvany, Zhou and Birker (1992); Bendsoe (1989), are commonly used to determine topology optimization designs. The homogenization model uses microscopic material distribution to find the optimum solution, whereas the SIMP method employs the pseudo density of each element as a design variable. Since the SIMP method implementation is relatively simpler and is more efficient than the homogenization model, this algorithm is usually preferred.

The SIMP technique can be successfully applied for multi-constraints, multi-materials, and multi- physics conditions. Through this method, the intermediate densities of each element (pseudo density (ρ_e)) are penalized to distinctive values near 0 (void) or 1 (solid), see Bendsoe and Sigmund (2003).

For an isotropic material, each element's Young's modulus matrix ($\mathbf{E}_e(\rho_e)$) is approximated as:

$$\mathbf{E}_e(\rho_e) = (\rho_e)^p \mathbf{E}_e^0; \quad 0 < \rho_{min} \leq \rho_e \leq 1 \tag{34}$$

where $\mathbf{E}_e^0$ and p are each element's Young's modulus matrix for a solid state material($\rho_e = 1$) and penalization factor, respectively. The minimum density value ($\rho_{min} = 0.01$) is mentioned in Eq. (35) in order to avoid singularity of the stiffness matrix during the FEM solution.

For a dynamic system, a mass matrix ($\mathbf{M}_e(\rho_e)$) is approximated as, see Du and Olhoff (2007):

$$\mathbf{M}_e(\rho_e) = (\rho_e)^q \mathbf{M}_e^0 \tag{35}$$

where $\mathbf{M}_e^0$represents the element mass matrix corresponding to the solid state material, and q is the penalization factor for the mass matrix (usually equal to 1).

For piezoelectric structures, these interpolations are applied on the three elements (c_E), (e), and (ε_s) (according to Eq. (2)) as, see Kim J.E., Kim D.S., Ma and Kim Y.Y. (2010):

$$c_E = f_c(\rho_e) c_E^0 \tag{36}$$

$$e = f_e(\rho_e) e^0 \tag{37}$$

$$\varepsilon_s = f_\varepsilon(\rho_e) \varepsilon_s^0 \tag{38}$$

wheref_c, f_e, and f_ε are the material coefficient interpolation functions, and c_E^0, e^0, and ε_s^0represent the nominal material matrices for the solid material case($\rho_e = 1$).

Based on the piezoelectric material with penalization and polarization (PEMAP-P) model, these interpolation coefficients can be written as, see Kim J.E., Kim D.S., Ma and Kim Y.Y. (2010):

$$f_c(\rho_e) = \rho_e^{nc}; \quad f_e(\rho_e) = \rho_e^{ne}; \quad f_\varepsilon(\rho_e, \gamma_e) = \rho_e^{n\varepsilon}(2\gamma_e - 1)^{np} \tag{39}$$

where the exponents nc, ne,and $n\varepsilon$ are the material density penalization factors, and np is the penalization power for the polarization variable (γ_e). By ignoring the effect of polarization, this equation leads to, see Kim J.E., Kim D.S., Ma and Kim Y.Y. (2010):

$$f_c(\rho_e) = \rho_e^{nc}; \quad f_e(\rho_e) = \rho_e^{ne}; \quad f_\varepsilon(\rho_e) = \rho_e^{n\varepsilon}. \tag{40}$$

Finding appropriate penalization powers is usually based on a numerical trial and error process; see Bendsoe and Sigmund (1999).

4.1 Sensitivity Analysis

Sensitivity analysis is usually a critical procedure in optimization problems.

During the design variable updating process (such as the MMA optimizer), calculation of the objective function ($ObjectFun$) and related constraints differentiations with respect to design variables (ρ_e) is necessary. Here, this sensitivity analysis is conducted via an efficient method called the adjoint sensitivity analysis; see Choi and Kim (2005).

For a dynamic system, an objective function can be defined using a real function ($ObjectFun_0$) as, see Jensen (2009):

$$ObjectFun = ObjectFun_0(\rho, \hat{\mathbf{u}}_r, \hat{\mathbf{u}}_i) \tag{41}$$

where $\hat{\mathbf{u}}_r$ and $\hat{\mathbf{u}}_i$ are the real part and imaginary parts of the displacement vector, respectively. By introducing the Lagrangian multiplier (λ), the adjoint form of this function becomes:

$$ObjectFun = ObjectFun_0(\rho, \hat{u}_r, \hat{u}_i) + \lambda^T(\tilde{G}\hat{u} - f) + \bar{\lambda}^T(\bar{\tilde{G}}\bar{\hat{u}} - \bar{f}) \tag{42}$$

where the over bar items in Eq. (43) denote the complex conjugates.

Based on Jensen's note in 2009, the final sensitivity expression then is:

$$\frac{\mathrm{d}(ObjectFun)}{\mathrm{d}\rho_e} = \frac{\partial(ObjectFun_0)}{\partial\rho_e} + 2Real\left[\lambda^{\mathrm{T}}\left(\frac{\partial\tilde{\mathbf{G}}}{\partial\rho_e}\hat{\mathbf{u}} - \frac{\partial\mathbf{f}}{\partial\rho_e}\right)\right] \tag{43}$$

where (λ) is the solution to:

$$\tilde{\mathbf{G}}\lambda = -\frac{1}{2}\left[\frac{\partial(ObjectFun_0)}{\partial \hat{\mathbf{u}}_r} - \mathrm{i}\frac{\partial(ObjectFun_0)}{\partial \hat{\mathbf{u}}_i}\right]^{\mathrm{T}}. \tag{44}$$

For these systems:

$$\frac{\partial \tilde{\mathbf{G}}}{\partial \rho_e} = -w^2\frac{\partial \tilde{\mathbf{M}}}{\partial \rho_e} + \mathrm{i}w\frac{\partial \tilde{\mathbf{C}}}{\partial \rho_e} + \frac{\partial \tilde{\mathbf{K}}}{\partial \rho_e}. \tag{45}$$

The components of this equation for piezoelectric materials and by a proportional damping assumption can be approximated by the SIMP method as, see Kim J.E., Kim D.S., Ma and Kim Y.Y. (2010); Du and Olhoff (2007):

$$\frac{\partial \tilde{\mathbf{M}}}{\partial \rho_e} = \begin{cases} \tilde{\mathbf{M}}_e^0 & \rho_e > 0.1 \\ 6c_0\rho_e^5\tilde{\mathbf{M}}_e^0 & \rho_e \le 0.1 \ (c_0 = 10^5) \end{cases} \tag{46}$$

$$\frac{\partial \tilde{\mathbf{K}}}{\partial \rho_e} = \begin{bmatrix} \frac{\partial \tilde{\mathbf{K}}_{e(uu)}}{\partial \rho_e} & \frac{\partial \tilde{\mathbf{K}}_{e(u\varphi)}}{\partial \rho_e} \\ \frac{\partial \tilde{\mathbf{K}}_{e(u\varphi)}}{\partial \rho_e} & \frac{\partial \tilde{\mathbf{K}}_{e(\varphi\varphi)}}{\partial \rho_e} \end{bmatrix} = \begin{bmatrix} nc(\rho_e)^{nc-1}\tilde{\mathbf{K}}^0_{e(uu)} & ne(\rho_e)^{ne-1}\tilde{\mathbf{K}}^0_{e(u\varphi)} \\ ne(\rho_e)^{ne-1}\tilde{\mathbf{K}}^0_{e(u\varphi)} & n\varepsilon(\rho_e)^{n\varepsilon-1}\tilde{\mathbf{K}}^0_{e(\varphi\varphi)} \end{bmatrix} \tag{47}$$

$$\frac{\partial \tilde{\mathbf{C}}}{\partial \rho_e} = \alpha\frac{\partial \tilde{\mathbf{M}}}{\partial \rho_e} + \vartheta\frac{\partial \tilde{\mathbf{K}}}{\partial \rho_e} \tag{48}$$

where $(\tilde{.})_e^0$ denotes the element stiffness or mass smoothed matrices for the solid material sate.

5 Problem algorithm

The applied topology optimization algorithm for this study can be summarized in figure 6.

6 Numerical results and discussions

Numerical topology optimization results of the prescribed mechanism (according to figures 2 to 4) for various numerical methods will be examined and compared here, with some of these results further discussed at the end of this section. All computations were conducted on a PC using an *Intel® Core(TM) 2 Quad*, Q9550@2.83 *GHZ CPU*, and *4GB RAM*.

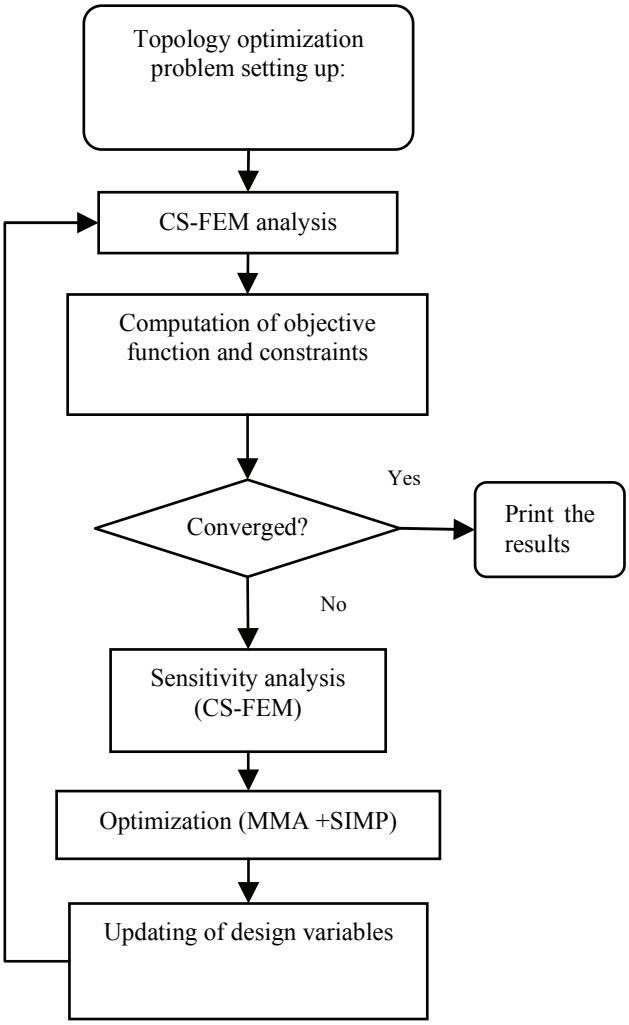

Figure 6: General applied DTO flow chart

6.1 Numerical results

6.1.1 Problem definition

The final goal of this study is to find an optimal material distribution required for a linear micromotor (shown in figure 2) to reach the maximum linear velocity. To that end, a set of proper objective function and constraints need to be defined.

According to Eq. (33) (for a constant excitation frequency), if the resultant end-

point displacement for each beam is maximized, the end-point velocity of this beam will be maximized. Hence, the final objective function can be defined to maximize the resultant end-point displacement of each microbeam (point (A) in figure 7 (b)). The matrix form of the objective function can thus be written as:

$$ObjectFun_0 = -\hat{\mathbf{u}}^T \mathbf{L} \bar{\hat{\mathbf{u}}} \tag{49}$$

where $\mathbf{L}$ is a diagonal matrix independent from the design variable whose non-zero diagonal entries are proportional to the position of point (A) in figure 7(b).

The configuration (including materials and polarization direction), design domain, and dimension of each beam are shown in figures 7(a), 7(b), and 8. The thickness of each beam is 1 (mm), applied voltage is 100 (volts) ($\mathbf{V_0} = 100(v)$), and the excitation frequency w is 1 Hz.

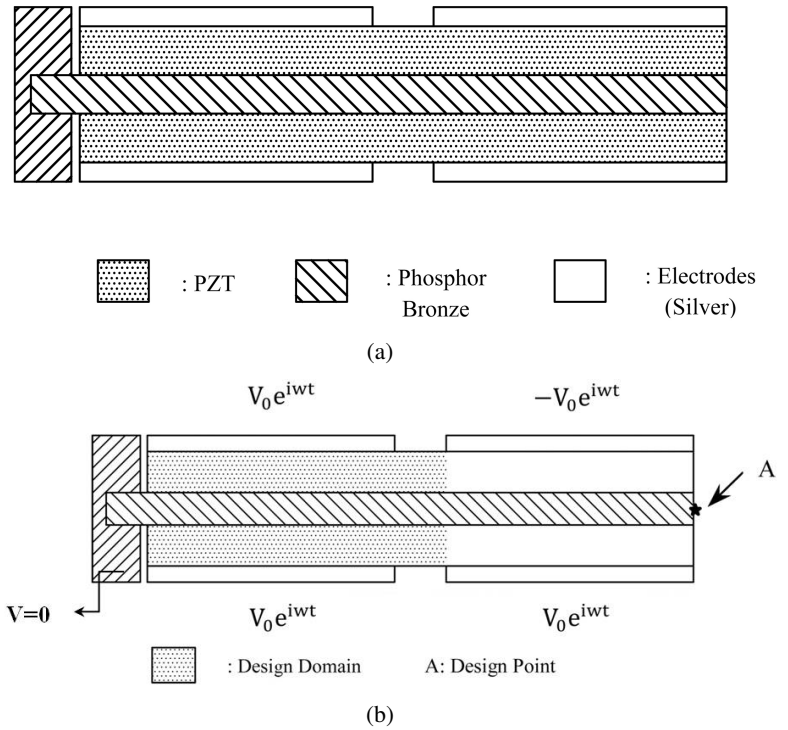

Figure 7: Definition of the problem: (a) general configuration and (b) design domain

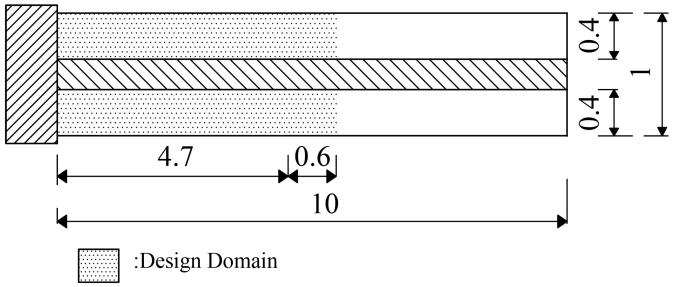

Figure 8: Dimension of the optimization problem (based on mm)

The setting of this problem can be summarized as follows:

$$\begin{cases} \text{Objective function: } -\hat{\mathbf{u}}^T \mathbf{L}\bar{\hat{\mathbf{u}}} \\ \text{Design variable: Pesudo density } (\rho_e) \end{cases} ; \tag{50}$$

$$\text{Subject to: } \begin{cases} \text{Equilibrium equations} \\ \frac{\sum_{e=1}^{num} Vol_e(\rho_e)}{Vol_0} \leq volfrac{=}50\% \\ 0 < \rho_{min} \leq \rho_e \leq 1 \end{cases}$$

where Vol_0 ,Vol_e, num and $volfrac$ are the volume of the design domain corresponding to $\rho_e = 1$, volume of each element, number of elements in the design domain, and the volume fraction ratio, respectively.

This problem is then analyzed using the following assumptions and parameters:

a. The problem condition is linear and quasi-static.

b. The thickness of each electrode is very small in comparison to dimensions of the other parts.

c. A mesh of elements is used.

d. Material properties of the PZT are obtained from reference; see Nguyen, Liu, Nguyen T.T and Nguyen C.T (2009).

6.1.2 Topology optimization results with 50% volume fraction

Using Eqs. (44) and (45), a sensitivity analysis for the above objective function (Eq. (50)) is calculated via the adjoint variable method as:

$$\frac{\mathrm{d}(-\hat{\mathbf{u}}^T \mathbf{L}\bar{\hat{\mathbf{u}}})}{\mathrm{d}\rho_e} = -2Real(\lambda^T \frac{\partial \tilde{\mathbf{G}}}{\partial \rho_e}\hat{\mathbf{u}}) \tag{51}$$

and

$$\tilde{\mathbf{G}}\lambda = \mathbf{L}^T\tilde{\mathbf{u}}. \tag{52}$$

The topology optimization results obtained using our procedure are listed in table 1.

The instantaneous velocity convergence rates and our topology optimization configurations are found using different approaches, as shown in figures 9(a) to 9(e) and figures 10(a) to 10(e).

Table 1: Comparison of our topology optimization designs with 50% volume fraction

FEM Analysis	Initial Instantaneous Velocity (mms^{-1})	Optimized Instantaneous Velocity (mms^{-1})	Number of Iterations	Total CPU Time (min)
Q4-FEM	0.0297	1.0625	278	60.1
T3-FEM	0.0249	0.7045	249	51.0
CS-FEM (*nSD=2*)	0.0329	1.4668	282	56.8
CS_FEM (*nSD=4*)	0.0304	1.1393	367	101.7
CS_FEM (*nSD=8*)	0.0299	1.1183	218	79.9

6.1.3 Reanalysis

Since topology optimization designs usually include gray zones (as can be observed in figure 10), these structures are not generally suitable for manufacturing. To improve this defect, a reanalysis process is executed at the end of the optimization procedure; see Bendsoe and Sigmund (2003). By applying this technique, the design variables (e.g., the pseudo density of each element) that are less than a threshold factor will be removed and the larger values will be approximated as the solid state condition ($\rho_e = 1$).

Based on this procedure, our final topology optimization results are listed in table 2, where the threshold factor is 0.6.

The reanalysis configurations of this design (figure (10)) are then determined using the FEMs and shown in figures 11(a) to 11(e).

6.2 Discussions

It has been shown that when the number of smoothing domains increases, the CS-FEM approaches the Q4-FEM results, see Liu, Dai and Nguyen (2007); Liu and

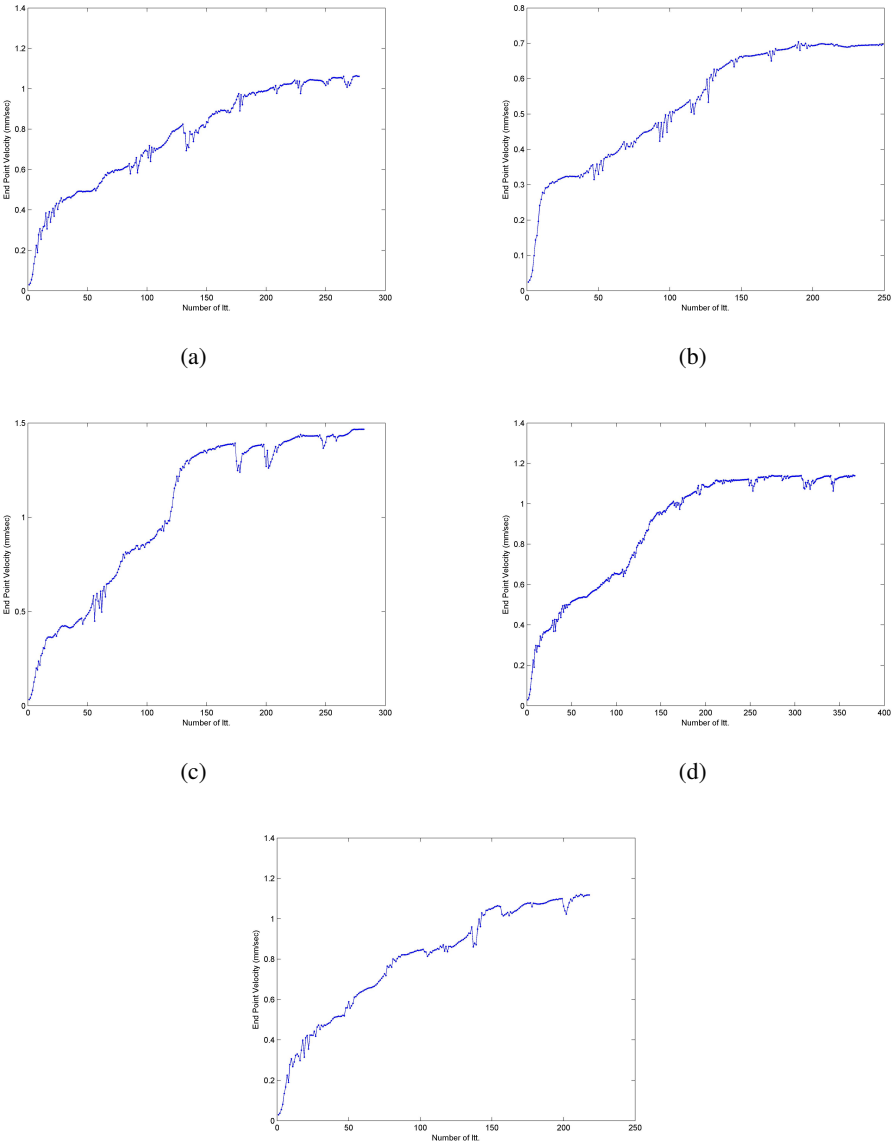

(a) (b)

(c) (d)

(e)

Figure 9: Topology optimization designs' velocity convergence rates (50% volume fraction) for: (a) Q4-FEM, (b) T3-FEM, (c) CS-FEM (*nSD=2*), (d) CS-FEM (*nSD=4*), and (e) CS-FEM (*nSD=8*)

Nguyen (2010); Liu, Nguyen, Dai and Lam (2007). This was also observed in the final results: when the number of smoothing domains was increased (from 2 to 8), the optimized velocity approached the Q4-FEM results. This observation provides, in a way, a validation of the CS-FEM for determining topology optimization designs when many smoothing domains are used.

From S-FEM theory, we know that the S-FEM model becomes stiffer with an increase of the smoothing domains. Therefore, by using fewer domains, we can obtain a softer CS-FEM model, and hence achieve a more accurate solution which is important for optimization problems, see Liu, Dai and Nguyen (2007); Liu and Nguyen (2010).

Because a smoothed strain is used inside each smoothing domain in the CS-FEM, by increasing the number of smoothing domains the final topology optimized results will have fewer checkerboard or gray regions than even the designs obtained by standard FEMs, see Huang and Xie (2010). Indeed, as can be observed from the obtained results, after the reanalysis process the optimized velocity for CS-FEM (*nSD=2*) is less than the velocity from CS-FEM (*nSD=4*).

In our study, because the final reanalysis optimal objective function (linear velocity) obtained through CS-FEM (*nSD*=4) has a higher value than the other designs (e.g., more than about 11% with respect to the Q4-FEM result), and because this method usually has a more reasonable accuracy respect to the other numerical methods (for this type of problem), see Liu and Nguyen (2010), we suggest that *nSD=4* leads to the optimal solution.

Table 2: Comparison of our final reanalysis designs (Threshold factor: 0.6)

FEM Analysis	Optimized Instantaneous Velocity (mms^{-1})	Volume Ratio (%)
Q4-FEM	0.588	0.479
T3-FEM	0.4318	0.487
CS-FEM (*nSD=2*)	0.4267	0.468
CS-FEM (*nSD=4*)	0.6558	0.482
CS-FEM (*nSD=8*)	0.585	0.477

7 Conclusions

Piezoelectric microactuators are extensively being used in industrial and medical science technologies. However, to attain even higher operational and economic efficiency, the optimum design of these structures is required.

Figure 10: Our topology optimization designs with 50% volume fraction for :(a) Q4-FEM, (b) T3-FEM, (c) CS-FEM (*nSD=2*), (d) CS-FEM (*nSD=4*) ,and (e) CS-FEM (*nSD=8*)

The topology optimization of a prescribed linear piezoelectric micromotor needed to reach maximum velocity by satisfying the 50% volume (weight) fraction and required equilibrium equations has been evaluated in this research. This optimization was determined using a softer cell-based smoothed FEM (as a branch of smoothed FEMs), and the results were then compared to standard FEMs. A comparison of the DTO results shows that the topology optimization design using the softer cell-based smoothed FEM, with *nSD=4*, is preferred.

The considered micromotor is currently being produced commercially, and it can substantially improve the efficiency of these piezoelectric micromotors.

Considering the possible reliability constraints during development of the optimum design of MEMS structures is recommended; most are due to inherent variations incurred during the manufacturing process. On the other hand, smoothed-FEMs are usually more effective for nonlinear systems. Hence, these types of optimizations using the S-FEM can be developed in the future.

(a) (b) (c) (d) (e)

Figure 11: Our reanalysis topology optimization designs for :(a) Q4-FEM, (b) T3-FEM, (c) CS-FEM (*nSD=2*), (d) CS-FEM (*nSD=4*), and (e) CS-FEM (*nSD=8*)

References

Allik, H.; Hughes, T. J. R. (1970): Finite element method for piezo-electric vibration, *Int. J. Numer. Meth. Eng.,* Vol. 2, pp. 151-157.

Arora, J.S. (2004): *Introduction to optimum design.* Second edition, Elsevier academic press.

Begg, D.W.; Liu. X. (2000): On simultaneous optimization of smart structures-Part II: Algorithms and examples. *Comput. Methods Appl. M.*, Vol. 184, pp. 25-37.

Bendsoe, M.P. (1989): Optimal shape design as a material distribution problem. *Struct. Optimization,* Vol. 1, pp.193-202.

Bendsoe, M.P.; Kikuchi, N. (1988): Generating optimal topologies in structural design using a homogenization method. *Comput. Methods Appl. M.*, Vol.71, pp.197-224.

Bendsoe, M.P.; Sigmund, O. (1999): Material interpolations in topology optimization. *Arch. Appl. Mech.*, Vol. 69, pp.635–654.

Bendsoe, M.P.; Sigmund, O. (2003): *Topology Optimization: Theory, Methods*

and Applications. Springer, Berlin.

Benjeddou, A. (2000): Advances in piezoelectric finite element modeling of adaptive structural elements: a survey. *Comput. Struct.,* Vol.76, pp. 347-363.

Bordas, S.P.A.; Rabczuk. T.; Hung, N.X.; Nguyen, V.P; Natarajan, S.; Bog, T.; Quan, D.M.; Hiep, N.V. (2010): Strain smoothing in FEM and XFEM. *Comput. Struct.*, Vol.88, pp.1419-1443.

Carbonari, R.C.; Nader, G.;Silva, E.C.N. (2006): Experimental and numerical characterization of piezoelectric mechanisms designed using topology optimization. *Int. ABCM symposium series in Mechatronics* ,Vol.2, pp.425-432.

Carbonari, R.C.; Silva, E.C.N.; Nishiwaki, S. (2005): Design of piezoelectric multi-actuated microtools using topology optimization. *Smart Mater. Struct.*, Vol.14 , pp. 1431-1447.

Chen, J.S.; Wu, C.T.; Yoon, S. Y. (2001): A stabilized conforming nodal integration for Galerkin mesh-free methods. *Int. J. Numer. Meth. Eng.*, Vol.50, pp.435-466.

Choi, K.K.; Kim, N.H. (2005): *Structural Sensitivity Analysis and Optimization*. Springer Science and Business Media, Inc., New York.

Dai, K.Y.; Liu, G.R.; Nguyen, T.T. (2007): An n-sided polygonal smoothed finite element method (nSFEM), for solid mechanics. *Finite Elem. Anal. Des.*, Vol.43, pp. 847-860.

Donoso, A.; Sigmund, O. (2009): Optimization of piezoelectric bimorph actuators with active damping for static and dynamic loads. *Struct. Multidiscip. O.*, Vol.38,pp.171-183.

Du, J.; Olhoff, N. (2007): Topological design of freely vibrating continuum structures for maximum values of simple and multiple eigenfrequencies and frequency gaps. *Struct. Multidiscip. O.*, Vol. 34, pp.91-110.

Frecker, M.I. (2003): Recent advances in optimization of smart structures and actuators. *J. Intel. Mat. Syst. Str.*, Vol. 14, pp.207-216.

Friend, J.; Umeshima, A.; Ishii, T.; Nakamura, K.; Ueha, S. (2004): A piezoelectric linear actuator formed from a multitude of bimorphs. *Sensor. Actuat. A-Phys.*, Vol. 109, pp. 242-251.

Huang, X.; Xie, Y.M. (2010): *Evolutionary Topology Optimization of Continuum Structures Methods and Applications*, John Wiley and Sons Ltd.

Irschik, H. (2002): A review on static and dynamic shape control of structures by piezoelectric actuation. *Eng. Struct.,* Vol.24 (1), pp.5-11.

Jensen, J. S. (2009): *A Note on Sensitivity Analysis of Linear Dynamic Systems*

with Harmonic Excitation, Report. Department of Mechanical Engineering, Technical University of Denmark.

Kang, Zh.; Wang, X. (2010): Topology optimization of bending actuators with multilayer piezoelectric Material. *Smart Mater. Struct.*, Vol.19, 075018(11p).

Kim, J.E.; Kim, D.S.; Ma, P.S.; Kim, Y.Y. (2010): Multi-physics interpolation for the topology optimization of piezoelectric systems. *Comput. Method. Appl. M.*, Vol.199, pp.3153-3168.

Kogl, M.; Silva, E.C.N. (2005): Topology optimization of smart structures: design of piezoelectric plate and shell actuators. *Smart Mater. Struct.* , Vol.14 , pp. 387–399.

Liu, G.R. (2009): *Meshfree Methods – Moving beyond the finite element method*. 2nd Edn., CRC Press.

Liu, G.R.; Dai, K.Y.; Lim, K.M.; Gu, Y.T. (2003): A radial point interpolation method for simulation of two- dimensional piezoelectric structures. *Smart Mater. Struct.,* Vol. 12, pp. 171-180.

Liu, G.R.; Dai, K.Y.; Nguyen, T.T. (2007): A smoothed finite element method for mechanics problems. *Comput. Mech.*, Vol.39, pp. 859-877.

Liu, G.R.; Nguyen, T. T. (2010): *Smoothed Finite Element Methods*, CRC press, Taylor and Francis group.

Liu, G.R.; Nguyen, T.T.; Dai, K. Y.; Lam, K.Y. (2007): Theoretical aspects of the smoothed finite element method (SFEM). *Int. J. Numer. Meth. Eng.*, Vo.71, pp.902-930.

Liu, G.R.; Nguyen, T. T. ; Lam, K.Y. (2009): An edge-based smoothed finite element method (ES-FEM) for static, free and force vibration analyses of solids .*J. Sound Vib.,*Vol. 320, pp. 1100-1130.

Liu, G.R.; Nguyen-X.H.; Nguyen, T.T. (2010): A theoretical study on the smoothed FEM (S-FEM) models: Properties, accuracy and convergence rates*, Int. J. Numer. Meth. Eng.*, Vol.84 (10), pp.1222-1256.

Long, C. S.; Loveday, P. W.; Groenwold, A. A. (2006): Planar four node piezoelectric with drilling degrees of freedom. *Int. J. Numer. Meth. Eng.,* Vol. 65, pp.1802-1830.

Moskalik, A.J.; Brei, D. (1999): Force-deflection behavior of piezoelectric C-block actuator arrays .*Smart Mater. Struct.* , Vol.8, pp. 531-543.

Nguyen, X.H.; Liu, G.R.; Nguyen, T.T.; Nguyen, C.T. (2009): An edge-based smoothed finite element method for analysis of two-dimensional piezoelectric structures. *Smart Mater. Struct.,* Vol.18 (6), 065015(12pp).

Nocedal, J. ; Wrigh, S.J. (2006): *Numerical optimization*, Second edition ,Springer.

Ohs, R. R.; Aluru, N. R. (2001): Meshless analysis of piezoelectric devices. *Comput. Mech.,* Vol.27, pp. 23-36.

Rozvany, G.; Zhou, M.; Birker, T. (1992): Generalized shape optimization without homogenization. *Struct. Optimization*, Vol. 4, pp.250-254.

Silva, E.C.N. (2003): Topology optimization applied to the design of linear piezoelectric motors, *Smart Mater. Struct.*, Vol. 14, pp.309-322.

Silva, R.C.N.; Kikuchi, N. (1999): Design of piezocomposite materials and piezoelectric transducers using topology optimization- part III. *Arch. Comput. Method E.,* Vol. 6, pp.305-329.

Spillers, W.R.; MacBain, K.M. (2009): *Structural optimization* , Springer science + Business media.

Svanberg, K. (1987): Method of moving asymptotes—a new method for structural optimization, *Int. J. Numer. Meth. Eng.*, Vol.24, pp.359-373.

Sze, K. Y.; Yang, X. M.; Yao, L. Q. (2004): Stabilized plane and axisymmetric piezoelectric finite element models. *Finite Elem. Anal. Des.* Vol. 40, pp. 1105-1122.

Ueha, S.; Tomikawa, Y. (1993): *Ultrasonic Motors-Theory and Applications*. Monographs in Electrical and Electronic Engineering, Vol.29, Clarendon Press, Oxford.

Wang, Q.M. ; Zhang, Q. ; Xu, B. ; Liu, R. ; Cross, L.E. (1999): Nonlinear piezoelectric behavior of ceramic bending mode actuators under strong electric fields. *J. Appl. Phys.*, Vol. 86(6), pp.3352-3360.

Yang, J. (2006): *Analysis of Piezoelectric Devices*, World Scientific Publishing Co. Pte. Ltd.